Available online at www.sciencedirect.com
ScienceDirect
International Journal of Heat and Mass Transfer 51 (2008) 4940–4957
International Journal of HEAT and MASS TRANSFER
www.elsevier.com/locate/ijhmt

Analysis of wall-function approaches using two-equation turbulence models

X. Albets-Chico [a], C.D. Pérez-Segarra [a,*], A. Oliva [a], J. Bredberg [b]

[a] Centre Tecnològic de Transferència de Calor, Universitat Politècnica de Catalunya (UPC), ETSEIAT, C/ Colom, 11, 08222 Terrassa (Barcelona), Spain
[b] Multi-physics/CFD Epsilon, HighTech AB Lindholmspiren 9, SE-41756 Gothenburg, Sweden

Received 26 February 2007
Available online 28 April 2008

Abstract

This paper focuses the attention on the drawbacks and abilities of wall-function techniques through an analysis of well-known wall-functions from literature. Besides this, some deeper analysis of these tools by means of physical and numerical considerations are carried out in order to improve their limitations when they are applied to predict heat transfer and fluid flow. Accuracy, grid-sensitivity, numerical behaviour and verification of numerical simulations are key aspects in this paper. The main purpose is to obtain tools which are able to predict both fluid flow and heat transfer with low CPU time consumption, reduced grid-sensitivity and a relatively good accuracy.

Keywords: Wall-function; Two-equation; k–ϵ; k–ω; Grid-sensitivity; Blending

1. Introduction

This paper is focused on wall-function (WF) approaches applied over two-equation eddy-viscosity models. These approaches allow simulations using a moderate number of control volumes, which implies lower CPU times resources and smaller memory storage than other more general, but not always more accurate, approaches. This tendency has been recaptured for different authors in the last years, e.g., Craft et al. [1], Bredberg and Davidson [2], etc., which demonstrates a growing interest of turbulence modelling using WF treatments.

Taking into account limitations and special abilities of wall-function treatments, their analysis and development could be useful in many industrial cases, even working in combination with low Reynolds number (LRN) treatments (in multi-block approaches) depending on the nature of the expected flow in the different regions. The use of the law-of-the-wall can save important computational resources, making this treatment more interesting from an engineering point of view.

Grid-sensitivity is one of the most troublesome aspects related to wall-function treatments applied to CFD codes. Generally, CFD predictions are sensible to discretization. Different strategies, as grid-refinement, are useful to study this grid-dependent problem. However, wall-functions focus their attention on using large near-wall control volumes and, consequently, require alternative strategies to reduce mentioned drawback. They will be discussed.

Firstly, the near-wall cell position is a crucial aspect related to grid-sensitivity, since wall-function formulae are usually designed assuming near-wall cell is placed at logarithmic boundary-layer zone. What to do when (because of the discretization, the flow, etc.) the model has to work using near-wall cells placed out of the desired area is essential in order to reduce grid-sensitivity.

Secondly, the high Reynolds number (HRN) model used to solve inner nodes (those which are not located near the walls) also has an important influence on accuracy and grid-sensitivity. As the location of the second node and successive can be placed in any position of the turbulent

* Corresponding author. Tel.: +34 93 739 8192.
E-mail address: cttc@cttc.upc.edu (C.D. Pérez-Segarra).

0017-9310/$ - see front matter © 2008 Elsevier Ltd. All rights reserved.
doi:10.1016/j.ijheatmasstransfer.2008.03.002

Nomenclature

C_μ	turbulent model constant
c_p	specific heat at constant pressure
c_l	log-law constant ($c_\mathrm{l} = 2.44$)
C_f	friction factor
CV	control volume
D_h	hydraulic diameter
E, E^*	constants for velocity law-of-the-wall
$\widetilde{E}, \widetilde{E^*}$	constants for thermal law-of-the-wall
f_μ	damping function for low Reynolds number models
H	characteristic length (channel height or step height)
k	turbulent kinetic energy per unit mass
Nu	Nusselt number
P_k	production of k due to shear stresses
$\overline{P_k}$	near-wall averaged production of k due to shear stresses
σ	Prandtl number
$\bar{p}$	the mean pressure
p	accuracy estimator for Richardson extrapolation verification process
$\dot{q}_\mathrm{w}$	wall heat flux
Re_{D_h}	Reynolds number based on hydraulic diameter length and on bulk velocity ($Re_{D_\mathrm{h}} = \frac{\rho D_\mathrm{h} u_\mathrm{bulk}}{\mu}$)
Re_τ	Reynolds number based on channel mid-height length and friction velocity ($Re_\tau = \frac{\rho (H/2) u_\tau}{\mu}$)
Re_t	turbulent Reynolds number ($Re_\mathrm{t} = k/\nu\omega$ or $k^2/\nu\epsilon$)
$\overline{S_{ij}}$	mean rate of strain tensor
S_z	source term for generic turbulent dissipation (z) transport equation
$\overline{T}$	mean temperature
T'	turbulent fluctuating temperature
t	time
$\overline{u_i}$	mean velocity in the i-direction
u_i'	turbulent fluctuating velocity in the i-direction
u_τ	friction velocity ($u_\tau = \sqrt{\frac{\tau_\mathrm{w}}{\rho}}$)
$\rho\overline{u_i' u_j'}$	turbulent shear stress or *Reynolds stress tensor*
$\rho\overline{u_i' T'}$	turbulent heat flux
x_i	Cartesian coordinate in the i-direction
y^+	dimensionless distance to the nearest wall ($y^+ = \frac{y\rho u_\tau}{\mu}$)
y^*	dimensionless distance to the nearest wall ($y^* = \frac{y\rho\sqrt{k}}{\mu}$)

Greek symbols

α	thermal diffusivity (ν/σ)
δ_{ij}	Kronecker delta
ϵ	dissipation rate of k
$\tilde{\epsilon}$	corrected dissipation rate of k
η	numerical correction for WWF2 treatment
$\kappa, \kappa^*, \tilde{\kappa}$	constants for laws-of-the-wall
λ	thermal conductivity
μ	dynamic viscosity
μ_t	eddy or turbulent viscosity
μ_t^*	dimensionless eddy or turbulent viscosity ($\mu_\mathrm{t}^* = \mu_\mathrm{t}/\mu$)
ν	kinematic viscosity
π_k	dissipation term in turbulent kinetic energy transport equation
$\overline{\pi_k}$	near-wall averaged dissipation term in turbulent kinetic energy transport equation
π_z	dissipation term for generic turbulent dissipation (z) transport equation
Π	viscous to turbulent Prandtl ratio ($\Pi = \frac{\sigma}{\sigma_\mathrm{t}}$)
ρ	density
σ_T	turbulent Prandtl number
τ	turbulent time scale
τ_w	wall shear stress
τ^l	viscous shear stress
τ^t	turbulent shear stress
ξ	numerical correction for WWF2 treatment
ω	specific dissipation rate of k

Subscripts

avg	averaged
nw	near-wall
in	inlet
∞	main flow
h	hydraulic diameter
c	thermal viscous limit
w	wall
n	north face
p	main nodal value
v	viscous limit

Superscripts

p	relative to main node
N	relative to north node
H	relative to dimensionless distance
l	laminar or viscous
log	relative to logarithmic region
t	turbulent
vis	relative to viscous region

boundary layer (depending on the flow and the discretization), abilities of the mentioned HRN model are strongly related to the quality of the complete resolution of turbulent boundary layer. Regarding this fact, the way how k–ϵ and k–ω models impose boundary conditions at the wall is relevant, as further discussed.

2. Mathematical models

Performed analysis of wall-function (WF) treatments has been carried out through different k–ϵ and k–ω approaches. On the one hand, the simplified two-layer WF treatment proposed by Launder [3] has been chosen as the standard wall-function approach (hereafter called SWF1: standard wall function 1). Abilities of using $\sqrt{k}$ as velocity scale and its two-layer approach on modelization of the k-equation have been taken into account when trying to solve complex flows. Despite these improvements, this k–ϵ approach presents different problems. To overcome these problems, some modifications have been introduced in the standard approach (modified method is referred to SWF2: standard wall function 2). To solve inner nodes, both k–ϵ WF treatments use the classic high Reynolds number model described in [4].

On the other hand, k–ω treatments have been proposed taking into account different formulae, physical assumptions and corrections. The first one is based on physical considerations of Launder proposal [3] (which will be called WWF1: ω wall function 1), while the second is based on a "blending" between pure law-of-the-wall and viscous formulation based on y^*. Both new proposed k–ω treatments use the well-known two-equation k–ω high Reynolds number model by Wilcox [5].

The use of ω-equation instead of ϵ-equation is desirable because the former provides solutions for both the sublayer and the logarithmic regions, which is strongly related to grid-sensitivity, as shown.

2.1. Governing equations

The time-averaged governing equations (continuity, momentum and energy) of the fluid flow assuming: fluid Newtonian behaviour, constant thermophysical properties, non-participant radiant medium and negligible body forces, heat friction and influence of pressure on temperature, may be written in tensor notation as follows:

$$\frac{\partial \bar{u}_i}{\partial x_i} = 0 \tag{1}$$

$$\rho \frac{\partial \bar{u}_i}{\partial t} + \rho \bar{u}_j \frac{\partial \bar{u}_i}{\partial x_j} = -\frac{\partial \bar{p}}{\partial x_i} + \frac{\partial \tau_{ij}}{\partial x_j} \tag{2}$$

$$\rho \frac{\partial \overline{T}}{\partial t} + \rho \bar{u}_i \frac{\partial \overline{T}}{\partial x_i} = -\frac{1}{c_p} \frac{\partial \dot{q}_i}{\partial x_i} \tag{3}$$

where $\tau_{ij} = \mu(\frac{\partial \bar{u}_i}{\partial x_j} + \frac{\partial \bar{u}_j}{\partial x_i}) - \rho\overline{u_i' u_j'}$ and $\dot{q}_i = -\lambda \frac{\partial \overline{T}}{\partial x_i} + c_p \rho \overline{u_i' T'}$.

As has been noted previously, due to the time-averaging process of the Navier–Stokes equations, new terms have appeared in momentum and energy equations. They are the *Reynolds stress tensor* ($\rho\overline{u_i' u_j'}$) and the *turbulent heat flux* ($\rho\overline{u_i' T'}$). Using eddy-viscosity models these terms are modelled by analogy with the Stokes viscosity law and the Fourier heat conduction through the eddy-viscosity (μ_t) concept:

$$\rho\overline{u_i' u_j'} = -\mu_t \left(\frac{\partial \overline{u_i}}{\partial x_j} + \frac{\partial \overline{u_j}}{\partial x_i} \right) + \frac{2}{3} \rho k \delta_{ij} \tag{4}$$

$$\rho\overline{u_i' T'} = -\frac{\mu_t}{\sigma_T} \frac{\partial \overline{T}}{\partial x_i} \tag{5}$$

2.2. Strategies to address the wall-blocking effect: LRN and WF techniques

The wall-blocking effect is defined as the sudden relaminarization of the turbulent flow due to the proximity of a wall. Among two-equation eddy-viscosity models, there are two different and well-known strategies to address this effect: low Reynolds number (LRN) techniques and wall-function (WF) approaches. The former is based on damping effects over the turbulent equations, while the latter is developed under simplifications applied to the near-wall cell in combination with high Reynolds number models for inner nodes.

In this work, attention has been focussed on WF approaches, using for inner nodes different high Reynolds number two-equation models, depending on the dissipative variable (k–ϵ or k–ω treatments). The effort made on near-wall treatments is based on different assumptions and numerical corrections, as they will be shown.

On the other hand, low Reynolds number models are also tested and compared. With reference to drawbacks and abilities of WF techniques (reduction on memory storage and CPU time consumption, reduction on accuracy, numerical uncertainties, etc.), comparisons with the Ince–Launder k–ϵ LRN model [6] (hereafter called IL) and with Wilcox k–ω LRN model [7] (hereafter called WX93) will be of interest to quantify numerical and computational improvements of WF techniques.

2.3. LRN and HRN two-equation models implementation

Different high Reynolds number and low Reynolds number turbulence models are described by Eqs. (6)–(8). Models constants and damping functions have not been here included for brevity. They are clearly stated in original references: [4] for the high Reynolds number k–ϵ model; [5] for the high Reynolds number k–ω model; [6] for the low Reynolds number k–ϵ model (IL); and [7] for the low Reynolds number k–ω model (WX93):

$$\rho \frac{\partial k}{\partial t} + \rho \bar{u}_j \frac{\partial k}{\partial x_j} = \frac{\partial}{\partial x_j} \left[(\mu + \mu_t/\sigma_k) \frac{\partial k}{\partial x_j} \right] + P_k - \pi_k \tag{6}$$

$$\rho \frac{\partial z}{\partial t} + \rho \bar{u}_j \frac{\partial z}{\partial x_j} = \frac{\partial}{\partial x_j} \left[(\mu + \mu_t/\sigma_z) \frac{\partial z}{\partial x_j} \right] + P_z - \pi_z + S_z \tag{7}$$

$$\mu_t = \rho C_\mu f_\mu \frac{k^2}{\epsilon} \quad \text{or} \quad \mu_t = \rho f_\mu \frac{k}{\omega} \tag{8}$$

Details of the different terms can be found in the cited references. Generic dissipative variable (z) adopts three different forms depending on the model. The k–ϵ high Reynolds number model [4] uses the standard dissipation rate (ϵ)

while the LRN IL model [6] uses the "corrected" dissipation rate ($\tilde{\epsilon}$). On the other hand, the k–ω high Reynolds number model [5] and the WX93 model [7] employ the specific dissipation rate (ω). The "corrected" dissipation rate ($\tilde{\epsilon}$) is a numerical correction needed to enforce zero dissipation value at the wall ($\tilde{\epsilon}_w = 0$). Because of this, a "D" term in k-equation, which is the assumed value of ϵ at wall: $D = 2\nu\partial k^{1/2}/\partial x_j$, also needs to be added.

2.4. Near-wall treatments. The implementation and development of WF techniques

On the other hand, WF techniques are mainly defined by the specific near-wall treatment. Present work on implementation and development of WF techniques is based on the simplifications suggested by Launder in [3] over more complex two-layer approaches. In fact, this is the treatment defined as the "standard" approach in this work (although usually the work exposed in [4] is identified as the "standard" approach).

More concretely and from a general point of view, near-wall treatments are based on different mathematical formulae when a node is placed adjacent to a wall.

Instead of using the coupled set of Eqs. (1)–(8), near-wall treatments are based on simplifications which, carefully implemented, can lead to overcome the detailed resolution of the near-wall area.

The essence of these treatments is based on the simplification of N–S equations combined with Boussinesq hypothesis and mixing length assumption. These mathematics leads to the well-known law-of-the wall:

$$u = \frac{u_\tau}{\kappa}\ln y + \text{constant} \tag{9}$$

Further mathematical development and assumptions produce similar formulae for energy and turbulent variables. All these hypothesis are taken in logarithmic region and, because of this, the model has to be carefully designed and used within this zone (or not too far). This is an important aspect to achieve acceptable predictions of turbulent boundary layer.

2.5. Basic model: k–ϵ Launder treatment (standard wall function 1: SWF1)

This "standard" model is based on a two-layer assumption, i.e. to assume there is a limiting value (y_v) between the mainly viscous area ($y < y_v$) and the mainly turbulent area ($y > y_v$). This treatment is also plotted in Fig. 2. Due to the assumed physical behaviour, the numerical nature of the near-wall control volumes takes meaningfulness in order to implement the mathematical formulation. Essentially, there are three typical kinds of near-wall cells according to the region where they are situated: completely logarithmic, partially viscous, and completely viscous (Fig. 1a–c):

From Eq. (9), through mathematical repackaging and experimental adjusting, basic logarithmic equations are obtained [3]. In order to improve predictions under recirculating and separated flows, velocity friction in u^+ and y^+ is changed by $\sqrt{k} : u^* = u/\sqrt{k}$ and $y^* = y\sqrt{k}/\nu$. Thus, basic logarithmic equations are written as $u^* = \frac{1}{\kappa^*}\ln E^* y^*$ for velocity, and $T^* = \frac{\sigma_T}{\kappa^*}\ln \widetilde{E}^* y^*$ for temperature. They are used to describe the flow within the log-region (up to the viscous limit $y_v^* = \frac{\rho\sqrt{k}y}{\mu} = 20.4$). In the viscous sublayer, the fluid is close enough to the wall to completely decay turbulence.

Shear stress is hence described by $\tau_w = \frac{\mu}{y}u$ for the viscous sublayer, and $\tau_w = \frac{\kappa^*\rho\sqrt{k}}{\ln(E^* y^*)}u$ for the logarithmic area. Heat transfer modelling is analogously $\dot{q}_w = \frac{\lambda}{y}(T_w - T)$ for the viscous sublayer, and $\dot{q}_w = \frac{\kappa^*\rho\sqrt{k}}{\ln(E^* y^*)}(T_w - T)$ for the logarithmic region.

In order to close the formulation, E^* is obtained from $E^* = \frac{\exp(\kappa^* y_v^*)}{y_v^*}$, and $\widetilde{E}^*$ is calculated from Jayatillaka "pee-function" correlated from pipe flow [9]:

$$\widetilde{E} = \exp(\tilde{\kappa} y_c^+ \sigma)$$
$$\Re = 9.24(\Pi^{3/4} - 1)(1 + 0.28\exp(-0.007\Pi)); \quad \Pi = \frac{\sigma}{\sigma_t}$$

From these expressions, and considering that $\Re = \frac{\ln(E/E)}{\tilde{\kappa}}$, $y_c^+ = \frac{\ln E}{\tilde{\kappa}\sigma}$ and $y_c^* = C_\mu^{-1/4} y_c^+$ are obtained. Being (as Launder suggests [3]): $E = 9.8$, $\kappa = 0.41$, $E^* = 4.36$, $\kappa^* = 0.22$ and $\sigma_t = 0.9$, the set of equations are closed.

In concordance with assumptions made for heat transfer and fluid flow, the turbulence structure is also defined using

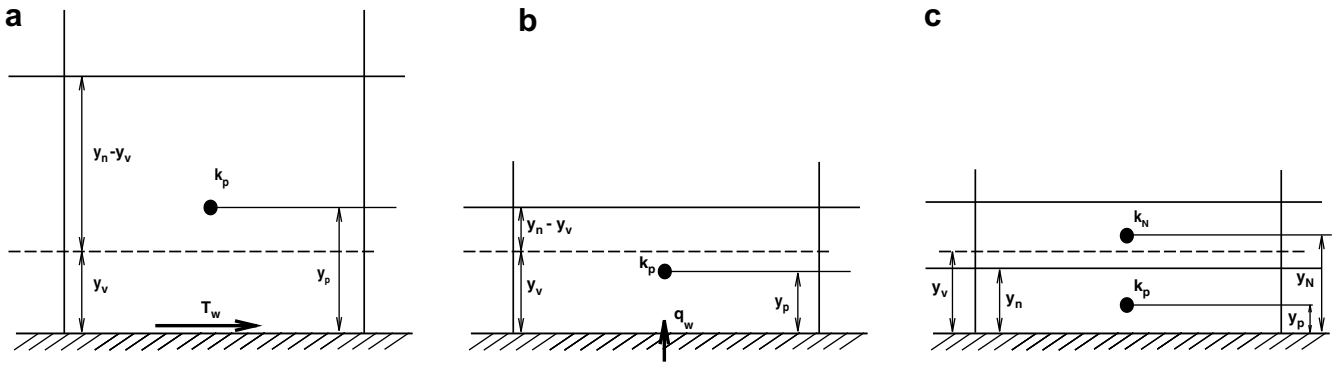

Fig. 1. Scheme of near-wall cell: (a) completely logarithmic; (b) partially viscous; (c) completely viscous.

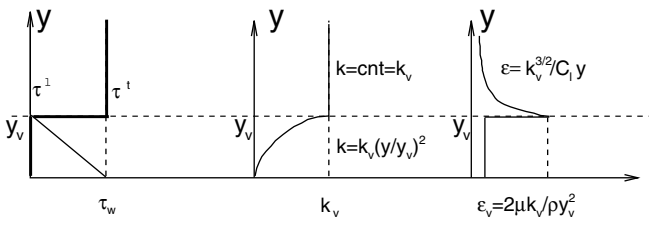

Fig. 2. Assumptions on near-wall turbulence structure for ϵ WF treatments.

a two-layer hypothesis. Fig. 2 shows assumptions made for k and ϵ profiles, as well as for viscous and turbulent shear stress distribution.

As the turbulent kinetic energy transport equation is solved at near-wall cells, Eq. (6) has to be slightly modified in order to capture physics of large control volumes. The local production (local P_k) and dissipation ($\pi_k = \rho\epsilon$) of turbulent kinetic energy are replaced by their averaged values ($\overline{P_k}$ and $\overline{\pi_k}$) based on a two-layer integration at the near-wall cell.

$\overline{P_k}$ is obtained under the two-layer integration, being the limiting value $y_v^* = 20.4$ and considering no turbulent kinetic energy production at sublayer ($\overline{P_k} = 0$ at $y < y_v$), as well as turbulent shear stress equal to the total shear stress ($\tau_w = \tau^l + \tau^t \approx \tau^t$ at $y > y_v$):

$$\overline{P_k} = \frac{1}{y_n}\left[\int_{y=0}^{y_v} P_k\,dy + \int_{y_v}^{y_n} P_k\,dy\right] \approx \frac{1}{y_n}\int_{y_v}^{y_n} P_k\,dy$$
$$\approx \frac{1}{y_n}\int_{y_v}^{y_n} \tau_w \frac{du}{dy}dy \approx \frac{\tau_w(u_n - u_v)}{y_n} \approx \frac{\tau_w^2/\rho}{\kappa^* y_n\sqrt{k}}\ln\frac{y_n}{y_v}$$

where the law-of-the-wall for velocities ($u_n - u_v = \frac{\tau_w/\rho}{\kappa^*\sqrt{k}}\ln\frac{y_n}{y_v}$) has been introduced.

Dissipation of turbulent kinetic energy is also treated using the two-layer assumption (see Fig. 2):

$$\overline{\pi_k}/\rho = \frac{1}{y_n}\left[\int_{y=0}^{y_v}\epsilon\,dy + \int_{y_v}^{y_n}\epsilon\,dy\right]$$
$$\approx \frac{2\mu k_v}{\rho y_n y_v} + \frac{1}{y_n}\int_{y_v}^{y_n}\frac{k_v^{3/2}}{c_l y}dy \approx \frac{2\mu k_v}{\rho y_n y_v} + \frac{k_v^{3/2}}{c_l y_n}\ln\frac{y_n}{y_v} \qquad (10)$$

Therefore, the turbulent kinetic energy equation (Eq. (6)) is solved using the above mentioned integrated $\overline{P_k}$ and $\overline{\pi_k}$ values (regarding Eq. (10), the standard approach implements $k_v = k_N$ when near-wall node is viscous and $k_v = k_p$ when near-wall node is placed in the logarithmic region, see Fig. 1). Integration is performed assuming zero diffusion of k at the wall, i.e. $\frac{\partial k}{\partial y}|_{y=0} = 0$. The dissipation rate of turbulent kinetic energy at the near-wall cell (ϵ_p) is obtained from the estimated profile (see Fig. 2) instead of the resolution of its own transport equation (Eq. (7)). Therefore, $\epsilon_p = \frac{2\mu k_N}{\rho y_v^2}$ when the near-wall node is under $y^* = 20.4$, and $\epsilon_p = \frac{k_p^{3/2}}{c_l y_p}$ when the near-wall node is placed in the logarithmic region. See Fig. 1 for more details. It is worth to say that the standard approach treats in the same way near-wall nodes placed in partially viscous or completely logarithmic areas, as $y_p^* > 20.4$ for both numerical configurations (SWF2 model will suggest some modifications about this subject, as shown). In order to close WF turbulence modelling, turbulent viscosity is obtained from Eq. (11) instead of Eq. (8) [3]:

$$\mu_t = \rho\kappa^* y_p\sqrt{k} \qquad (11)$$

2.6. Modifications on Launder treatment: k–ϵ (standard wall function 2: SWF2)

Due to grid-sensitivity troubles detected in the Launder treatment, some modifications are proposed. These changes reduce sensitivity of predictions regarding near-wall cell position. The main purpose is to improve behaviour of SWF1 model when near-wall cell is placed at viscous region, through modifications on formulation for both ϵ_p and ϵ_N. Other aspects are treated as in the SWF1 approach. $\overline{P_k}$ and $\overline{\pi_k}$ are defined in the same way as SWF1.

As to the ϵ profile, some modifications have been introduced in ϵ_N and ϵ_p values. When the near-wall node is partially viscous ($y_p^* < y_v^*$), the value of the dissipation is ($\epsilon_p = \frac{2\mu k_N}{\rho y_n y_v} + \frac{k_N^{3/2}}{c_l y_n}\ln\frac{y_n}{y_v}$). Regarding ϵ_N, its value is computed as $\frac{k_N^{3/2}}{c_l y_N}$ for near-wall nodes placed in both completely ($y_n^* < y_v^*$) and partially viscous ($y_p^* < y_v^*$) areas. See Fig. 1.

As can be seen, ϵ_p adopts the value of $\overline{\pi_k}/\rho$ (obtained through the two-layer integration) when near-wall node is partially or completely placed at viscous region, while ϵ_N is solved using the assumed logarithmic profile for ϵ (instead its own transport equation) in that case. These modifications improve results when near-wall node is placed at viscous regions, which makes the model less sensitive to near-wall position, as shown.

2.7. First k–ω approach for WF ("ω" wall function 1: WWF1)

This k–ω treatment is based on a transformation of the k–ϵ SWF1 model. In fact, the WWF1 approach is based on SWF1 considerations, modifying the way dissipation of turbulence kinetic energy is modelled by changing the dissipation rate (ϵ) to the specific dissipation rate (ω). Hence, terms as shear stress, heat transfer, $\overline{P_k}$ and eddy-viscosity are calculated in the same manner as SWF1; other terms, such as $\overline{\pi_k}$ and ω_p are derived from assumptions made on turbulence structure in the vicinity of the wall, which are in agreement with hypothesis made for ϵ, as shown in Fig. 3.

Obviously, this modification implies the use of a k–ω model in high Reynolds regions and different formulae to fix specific dissipation near the wall. The high Reynolds model used in this approach is suggested by Wilcox in [5] (see Section 2.3). As shown, grid-sensitivity of this model is notoriously reduced because of the use of ω (which

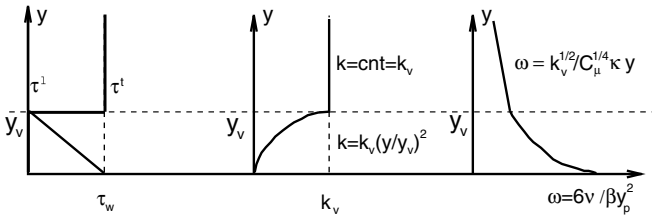

Fig. 3. Assumptions on near-wall turbulence structure for ω WF treatments.

provides both logarithmic and viscous solutions) when approaching to the wall.

With reference to turbulence modelling, previously two-layer exposed assumptions have been followed, hence $\overline{\pi_k}$ is obtained from integration. On the other hand, as to was done for ϵ, a different integration for logarithmic and viscous areas is herewith proposed. For logarithmic regions, an averaged dissipation rate of k ($C_\mu k\omega_{\text{avg}}$) is computed taking into account the derived law-of-the-wall for ω. It is interesting to note that viscous part ($\int_{y=0}^{y=y_v} C_\mu \omega k \,\mathrm{d}y$) has been removed, as it has been suggested by Bredberg [10] and ratified by computations, which have shown how this amount can be neglected without any significant influence on final results:

$$\begin{aligned}\overline{\pi_k}/\rho &= \frac{1}{y_n - y_v}\left[\int_{y_v}^{y_n} \epsilon \,\mathrm{d}y\right] = \frac{1}{y_n - y_v}\left[\int_{y_v}^{y_n} C_\mu \omega k \,\mathrm{d}y\right] \\ &= \frac{1}{y_n - y_v}\int_{y_v}^{y_n} C_\mu \frac{\sqrt{k}}{C_\mu^{1/4}\kappa y} k \,\mathrm{d}y \\ &= \frac{1}{y_n - y_v}\frac{C_\mu^{3/4} k_p^{3/2}}{\kappa}\ln\frac{y_n}{y_v} \end{aligned} \tag{12}$$

As for viscous areas, $\omega \to 6\nu/\beta y^2$ as $y \to 0$ [11], the integration becomes

$$\begin{aligned}\overline{\pi_k}/\rho &= \frac{1}{y_n}\left[\int_{y=0}^{y_n} \epsilon \,\mathrm{d}y\right] = \frac{1}{y_n}\int_{y=0}^{y_n} C_\mu \omega k \,\mathrm{d}y \\ &= \frac{C_\mu}{y_n}\int_{y=0}^{y_n} \omega k \,\mathrm{d}y = \frac{C_\mu}{y_n}\int_{y=0}^{y_n} \frac{6\nu}{\beta y^2} k_v \left(\frac{y}{y_v}\right)^2 \mathrm{d}y \\ &= \frac{C_\mu}{y_n}\int_{y=0}^{y_n} \frac{6\nu}{\beta y_v^2} k_v \,\mathrm{d}y \approx C_\mu \frac{6\nu}{\beta y_p^2} k_p \end{aligned} \tag{13}$$

where the last approximation is based on the fact that $k_v/y_v^2 \approx k_p/y_p^2$ (see Fig. 2). Related to the nodal value for ω_p, the same considerations are used, leading to $\omega_p = \frac{\sqrt{k}\cdot\ln(y_n/y_v)}{C_\mu^{1/4}\kappa(y_n - y_v)}$ for logarithmic regions and to $\omega_p = \frac{6\nu}{\beta y_p^2}$ for viscous areas.

Finally, and in order to close WWF1 near-wall implementation details, it is important to note a different interpolation for eddy-viscosity. To obtain a value for the eddy-viscosity at limiting surface of the near-wall control volume (μ_t^n), the most usual practice is to apply a linear interpolation between near-wall cell (μ_t^P) and inner cell (μ_t^N). This approach, however, applies a pseudo-harmonic interpolation in order to reproduce the wall-damping effect, since this formulation reduces μ_t^n (and consequently, τ^n and due to momentum conservation, τ_w) when near-wall node is placed at buffer-layer. Despite the obtention of some unrealistic profiles, this term allows to improve accuracy of the method. The interpolation scheme is exposed in Eq. (14):

$$\mu_t^n = \left[\frac{1 - f_e}{\mu_t^P} + \frac{f_e}{\mu_t^N}\right]^{-1} \quad \text{where } f_e = \frac{y_n - y_p}{y_N - y_p} \quad \text{(see Fig.1)} \tag{14}$$

Diffusion of k to the wall is again fixed to zero and turbulent viscosity is fixed by means of Eq. (11).

2.8. Second k–ω approach for WF ("ω" wall function 2: WWF2)

Based on similar assumptions, a modified near-wall k–ω treatment is proposed. Attempting to improve the accuracy and to reduce the grid-sensitivity of previous near-wall approaches, a new blending near-wall treatment is suggested. The main idea is to blend pure viscous formulation and pure logarithmic formulation, and through a turbulence-sensible blending function, a modification of mathematical formulation is achieved. This fact allows to adapt near-wall cell computations to its physics. The blending has been designed as a function of y^*. This variable offers physical information on the location of the near-wall cell, which is appropriate in order to design the specific near-wall treatment. Additionally, this variable does not vanish under separated flow (as y^+ does) which allows resolution of these kinds of flows.

While previous approaches were built on a discrete switch between viscous and logarithmic formulation (placed at y_v), the essence of this attempt is to achieve a continuous adaptation of the mathematical formulation. Besides this aspect, and also motivated by it, more complete formulation is used to define the viscous sublayer, avoiding previous simplifications, which were more or less related to numerical problems.

The blending function (A) has been designed taking as reference the "theoretical" value for $y_v^* = 20.4$. Additionally, a numerical adjustment has been needed to refine sensitivity and accuracy of the proposal:

$$A = 1 - \exp\left[\frac{12 - y^*}{3}\right] \tag{15}$$

As shown in Fig. 4, the blending factor is almost 0 (pure viscous formulation) at $y^* \leqslant 12$, while it becomes 1 (pure logarithmic formulation) approximately at $y^* \geqslant 30$. Its value at $y_v^* = 20.4$ is of approximately 0.94. $A = 0.5$ is achieved at $y^* \approx 14$. As shown, this function rapidly goes to logarithmic formulation, which is more stable than viscous formulation at buffer-layer. To remove inaccuracies due to this fact, some numerical corrections will be proposed.

Shear stress and heat flux are described in Table 1. As can be seen, standard formulation is used for pure viscous

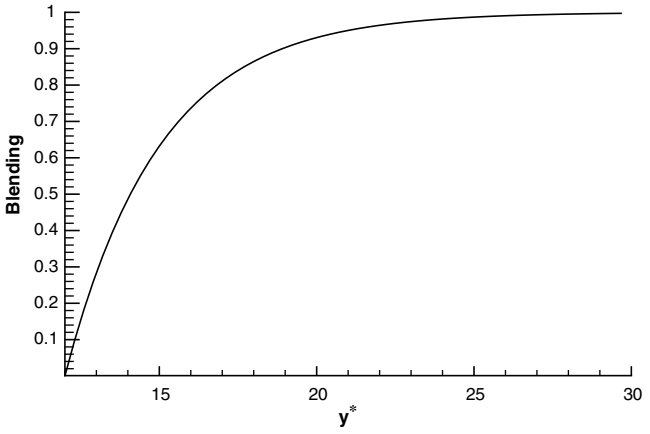

Fig. 4. WWF2 blending function.

Table 1
WWF2 near-wall flow modelling

Position of near-wall cell	τ_w	$\dot{q}_w$
Viscous ($y^* < 12$) ($y^* < y_c^*$)	$\frac{\mu}{y}u$	$\frac{\lambda}{y}(T_w - T)$
Transition ($12 < y^* < 30$)	$(1-A)\cdot\frac{\mu}{y}u + A\cdot\frac{\kappa^*\rho\sqrt{k}}{\ln(E^*y^*)}u$	–
Logarithmic ($y^* > 30$) ($y^* > y_c^*$)	$\frac{\kappa^*\rho\sqrt{k}}{\ln(E^*y^*)}u$	$\frac{\kappa^*\rho\sqrt{k}}{\ln(E^*y^*)}(T_w - T)$

Table 2
WWF2 $\overline{P_k}$ modelling depending on situation of near-wall node

Position of near-wall cell	$\overline{P_k}$
Viscous ($y^* < 12^*$)	$-\mu_t(\frac{\partial\overline{u_i}}{\partial x_j}+\frac{\partial\overline{u_j}}{\partial x_i})\frac{\partial\overline{u_i}}{\partial x_j}\cdot\eta$
Transition ($12 < y^* < 30$)	$(1-A)\cdot -\mu_t(\frac{\partial\overline{u_i}}{\partial x_j}+\frac{\partial\overline{u_j}}{\partial x_i})\frac{\partial\overline{u_i}}{\partial x_j}\cdot\eta + A\cdot\frac{\tau_w^2/\rho}{\kappa^* y_n\sqrt{k_N}}\ln\frac{y_n}{y_v}$
Logarithmic ($y^* > 30$)	$\frac{\tau_w^2/\rho}{\kappa^* y_n\sqrt{k_p}}\ln\frac{y_n}{y_v}$

and logarithmic parts, using a continuous transition between $y^* = 12$ and $y^* = 30$. The limiting values have been chosen using a combination of physical reasoning and numerical adjustment. Due to the Prandtl-dependence of the y_c^+ value and of the thermal law-of-the-wall, blending is not applied to the heat transfer computations.

As far as turbulence modelling is concerned, essential assumptions used on previous k–ω treatments are also adopted for this approach. Identical blending function is used for $\overline{P_k}$, $\overline{\pi_k}$ and ω_p computations. Moreover, and based on the use of the blending function, an exact P_k^{vis} formulation is adopted, instead of its suppression (as it was done in previous approaches). This term can be significant depending on the flow. Complete formulation of this term, $P_k^{vis} = \rho\overline{u_i'u_j'}\frac{\partial\overline{u}_i}{\partial x_j} = \tau_{ij}\frac{\partial\overline{u}_i}{\partial x_j}$, is described in Table 2.

Related to formulation for $\overline{\pi_k}$ and ω_p, the same considerations are carried out. Tables 3 and 4, respectively, show detailed mathematical formulation.

It is interesting to note the use of η-function for P_k^{vis} formulation and ξ-function for viscous $\overline{\pi_k} - \omega_p$ approaches. Both functions are numerical corrections suggested to improve the accuracy of the proposals when trying to perform the wall-blocking effect. One of the most difficult

Table 3
WWF2 $\overline{\pi_k}$ modelling depending on situation of near-wall node

Position of near-wall cell	$\overline{\pi_k}$
Viscous ($y^* < 12^*$)	$C_\mu\frac{6\nu}{\beta y_p^2}k_p\cdot\xi$
Transition ($12 < y^* < 30$)	$(1-A)\cdot C_\mu\frac{6\nu}{\beta y_p^2}k_p\cdot\xi + A\cdot\frac{1}{y_n-y_v}\frac{C_\mu^{3/4}k_p^{3/2}}{\kappa}\ln\frac{y_n}{y_v}$
Logarithmic ($y^* > 30$)	$\frac{1}{y_n-y_v}\frac{C_\mu^{3/4}k_p^{3/2}}{\kappa}\ln\frac{y_n}{y_v}$

Table 4
Node value of ω_p for WWF2 model depending on situation of near-wall node

Position of near-wall cell	ω_p
Viscous ($y^* < 12^*$)	$\frac{6\nu}{\beta y_p^2}\cdot\xi$
Transition ($12 < y^* < 30$)	$(1-A)\cdot\frac{6\nu}{\beta y_p^2}\cdot\xi + A\cdot\frac{\sqrt{k_p}\ln\frac{y_n}{y_v}}{C_\mu^{1/4}\kappa(y_n-y_v)}$
Logarithmic ($y^* > 30$)	$\frac{\sqrt{k_p}\ln\frac{y_n}{y_v}}{C_\mu^{1/4}\kappa(y_n-y_v)}$

problems when trying to achieve grid-insensitiveness is the modelization of the buffer-layer. This region is placed between the viscous sublayer and the inner or logarithmic layer. In the buffer-layer wall-damping effects are significant, which are responsible for the rapid decay of turbulence towards the wall.

η-function is based on the work of Bredberg [2] and is useful to "dampen" P_k^{vis} numerical inaccuracies due to the usual computation $\partial\overline{u_i}/\partial x_i \approx \Delta\overline{u_i}/\Delta x_i$. Eq. (16) makes such formulation up to $y^+ \approx 10$ viable, which is interesting in order to blend P_k^{vis} with P_k^{log} at buffer-layer. On the other hand, ξ-function is an alternative way to reproduce the wall-blocking effect, by multiplying by a factor of two ω_p and $\overline{\pi_k}$ between $y^* = 1$ and $y^* = 10$, i.e. the beginning of the buffer-layer. η and ξ are defined by Eqs. (16) and (17), respectively:

$$\eta = \frac{1}{1 + 0.9Re_t} \tag{16}$$

$$\xi = 2 - \left[\frac{5.5 - y^*}{4.5}\right]^8 \tag{17}$$

Unlike in previous near-wall treatments, the turbulent viscosity is based on the standard two-equation formula instead of the Prandtl–Kolmogorov expression. This is in agreement with the use of pure viscous formulation. Hence, $\mu_t = \rho k/\omega$ is used in this approach. In order to close the near-wall treatment, k-diffusion is also blocked to the wall ($\frac{\partial k}{\partial y}|_{y=0} = 0$).

3. Numerical aspects

3.1. Numerical procedure

The set of governing partial differential equations has been solved using finite volume techniques over a staggered discretization (where velocities are calculated on the control volume faces). A structured grid has been used. Fully implicit time integration has been applied, and a pressure

based method of the SIMPLE family (semi-implicit method for pressure-linked equations) [12] is used to solve the velocity–pressure field coupling. Central differences are employed for the evaluation of diffusion terms, and convective terms are discretized by means of UPWIND and SMART schemes for channel flow and UPWIND and Power-Law schemes for backward flow. A multi-grid iterative solver is used to solve the algebraic linear system of equations. For k and $\epsilon/\tilde{\epsilon}$ or ω equations source terms have been linearised in the usual form [12] to assume inconditional positive values avoiding numerical instabilities. All simulations have been carried out using a pseudo-transient iterative algorithm, applying the biggest time-step which ensures convergence, which, as has been shown, has depended on the case and the model.

3.2. Numerical solutions verification

A post-processing procedure, based on generalized Richardson extrapolation for *h-refinement* studies and on the grid convergence index (GCI) proposed by Roache [13] has been used in order to verify the numerical results provided by the continuous (LRN) models analysed in this work.

This technique is useful in order to establish criteria about the sensitivity of the simulation to the computational model parameters that account for the discretization: the mesh spacing and the order of accuracy of the numerical solutions (observed order of accuracy p). The error band where the independent grid solution is expected to be contained (uncertainty due to discretization GCI), and criteria on the credibility of these estimations are also achieved by this process. Local estimators of the GCI and p are calculated at the grid nodes where its evaluation has been possible. These grid nodes are called *Richardson nodes*. Global values of GCI and p are calculated by means of volumetric averaging. It is considered that an estimation is credible when the global observed order of accuracy p approaches its theoretical value, and when the number of *Richardson nodes* is high enough. See [13] for details.

WF techniques do not allow this rigorous post-processing verification procedure because of basically two reasons. Firstly, specific near-wall treatments are built on point-dependent formulation (mathematical formulation depends on the grid, so it cannot be verified by grid-refinement since formulation can change as the refinement is applied). Secondly, the grid-refinement needed to apply these tools cannot be directly applied in WF techniques, which are designed to work relatively far from the wall, avoiding the fine resolution required by LRN techniques. Hence, numerical inaccuracies related to WF techniques remain mixed with mathematical (related to model) inaccuracies. However, the latter are expected to be greater than the former. In fact, all meshes applied to test WF treatments have been designed using ratios $\Delta y_{nw}/\Delta y_{in} \approx 1$ (near-wall cell normal distance over first inner node normal distance), avoiding numerical diffusion.

4. Test cases and results

In order to compare, analyse and develop turbulence modelling by means of WF treatments, different cases have been tested.

A channel flow at moderate Reynolds number ($Re_\tau = 590$, $Re_{D_h} \approx 43,000$) [14] (see Fig. 5a), has been studied to check grid-sensitivity and aspects of modelling of physics for developed approaches.

A backward facing step flow (BFS) [15] at Reynolds number of $Re_H = 37{,}500$ (based on step height H and on inlet velocity $\bar{u}_\infty$) has been considered to test model abilities to solve reattached and separated flows (Fig. 5b). At the same time, this is an interesting test to evaluate grid-sensitivity of WF approaches, since the case presents different kinds of near-wall cells (from y^+ at logarithmic region until typical viscous near-wall cells).

Additionally, both cases have allowed significant comparisons to quantify the relative computational savings and improvements of WF techniques over LRN treatments.

4.1. Boundary conditions

The inlet conditions for test cases selected are formally identical. For channel flow, after different intents to reproduce the friction Reynolds number of $Re_\tau = 590$ (since this evaluation depends on the response of the model) an acceptable equivalence has been fixed using $Re_{D_h} = 43,000$ ($\bar{u}_{in} = \frac{\nu Re_{D_h}}{D_h}$), in addition to a turbulence intensity

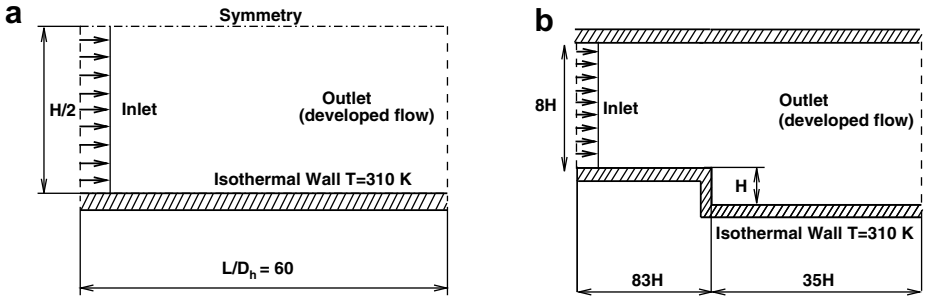

Fig. 5. (a) Channel and (b) backward facing step test cases.

of 7% ($k_{in} = 0.07^2\bar{u}_{in}^2$), and a dissipation rate $\epsilon_{in} = \frac{C_\mu k_{in}^{3/2}}{0.03H/2}$ or specific dissipation rate of $\omega_{in} = \frac{\epsilon_{in}}{C_\mu k_{in}}$. Inlet temperature has been fixed at $T_{in} = 300$ K to check heat transfer aspects.

As far as BFS is concerned, the imposition of the inlet conditions has been more intricate. Driver et al. [15] describes flow conditions at a location four step-heights upstream of the step. Consequently, to obtain desired upstream conditions, is the first aspect to solve. For this, a channel flow has been developed and adjusted in order to provide the desired inlet conditions for the BFS, this is, the reported experimental inlet conditions.

This profile could be imposed at the inlet of the BFS, saving the coupled resolution of the channel and the BFS and, therefore, economising mesh and computational requirements. However, and in order to simplify numerical computations and to check numerical improvements of WF techniques, the complete backward (plus channel) has been computed, as Fig. 5b shows. The complete case is, from an engineering point of view, more realistic and it will focus on some problems of LRN techniques which can be mitigated by using WF approaches.

Therefore, the inlet conditions for the BFS test case are those that generate a channel flow which reproduces the expected BFS inlet (at location four step-heights upstream the step). Hence, a constant inlet velocity profile is fixed at 95% of the reported mean stream velocity four step-heights upstream of the step ($\bar{u}_{in} = 0.95\bar{u}_\infty$). The turbulence intensity has been fixed at 3% ($k_{in} = 0.03^2\bar{u}_{in}^2$), while the dissipation rate is $\epsilon_{in} = \frac{5}{9}\frac{C_\mu k_{in}^{3/2}}{0.03H_{ch}/2}$ (for k–ω models $\omega_{in} = \frac{\epsilon_{in}}{C_\mu k_{in}}$). Finally, related to heat transfer computations, inlet temperature has been fixed at $T_{in} = 300$ K.

For both cases, a "developed flow" outlet boundary condition has been used, applying a null-gradient for T, k and $\tilde{\epsilon}$, ϵ or ω. Normal velocity is obtained from a mass balance for channel flow computations (fixing tangential velocity to 0). Whilst, for BFS flow, normal velocity is derived from an extrapolation of momentum equation from inner nodes, and tangential velocity is obtained from a null-gradient imposition.

Walls for both cases have also been considered isothermal at $T_{wall} = 310$ K, ensuring heat transfer between them and the flow.

4.2. Channel flow

With reference to channel flow, velocity and turbulent profiles are analysed to evaluate grid-sensitivity and accuracy of presented approaches. In order to assess skills and drawbacks related to present treatments, different grids have been used. To test WF methods, a wide range of spatial discretizations has been applied: from near-wall cells placed at $y^+ < 0.05$ (typical fine LRN mesh) up to locations of $y^+ \approx 100.0$ (limiting value for logarithmic region). This wide range of meshes can be observed in different plots herewith presented.

On the other hand, for LRN techniques, a grid-refinement methodology has been used (see Section 3.2). Five different meshes have been considered, ensuring through verification estimators the achievement of asymptotic results.

4.2.1. WF computations

Standard approach (SWF1) and k–ϵ modification (SWF2) fail when near-wall node is placed at viscous regions (see Fig. 6). Important discrepancies take place when determining turbulent kinetic energy at viscous layer (which can be seen in Fig. 8). Both models fail to predict length-scales through ϵ_p. Despite improvements achieved by SWF2 treatment when using near-wall nodes placed at buffer-layer and viscous sublayer, their predictions are not

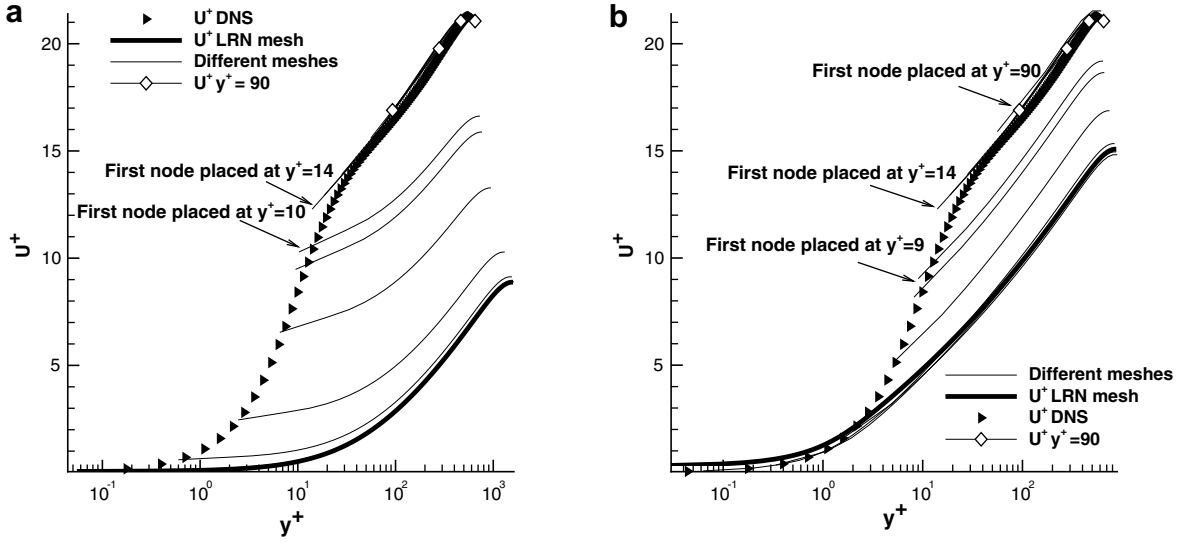

Fig. 6. Grid-sensitivity for the velocity profile ($u^+ = u/u_\tau$) over wall distance ($y^+ = yu_\tau/\nu$) and comparison to DNS data [14]. Channel flow ($Re_\tau = 590$). (a) SWF1 model; (b) SWF2 model.

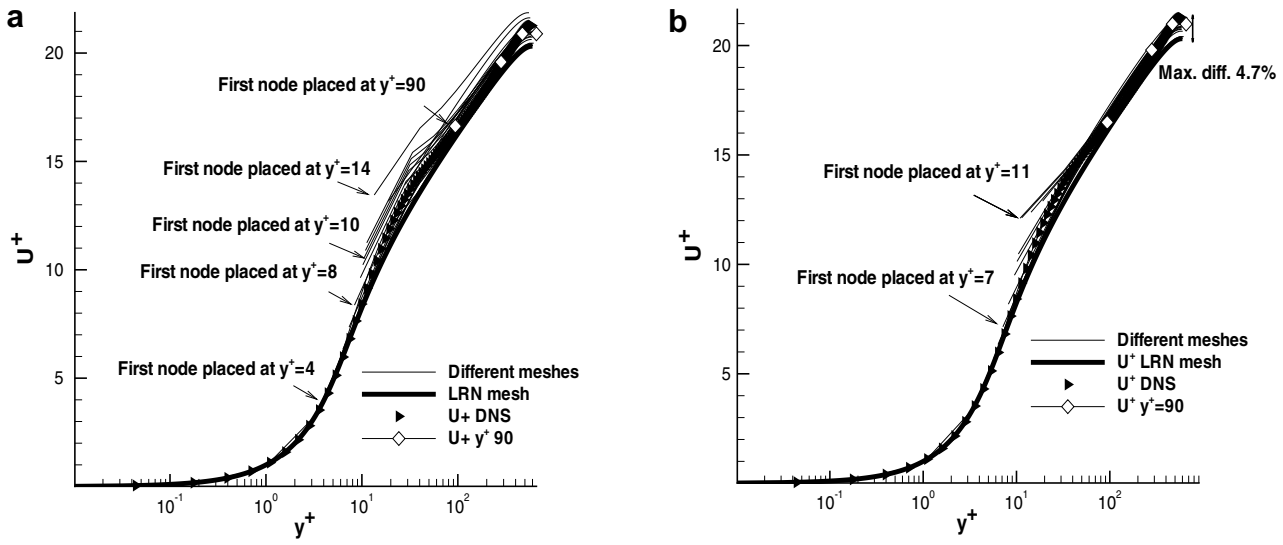

Fig. 7. Grid-sensitivity for the velocity profile ($u^+ = u/u_\tau$) over wall distance ($y^+ = yu_\tau/\nu$) and comparison to DNS data [14]. Channel flow ($Re_\tau = 590$). (a) WWF1 model; (b) WWF2 model.

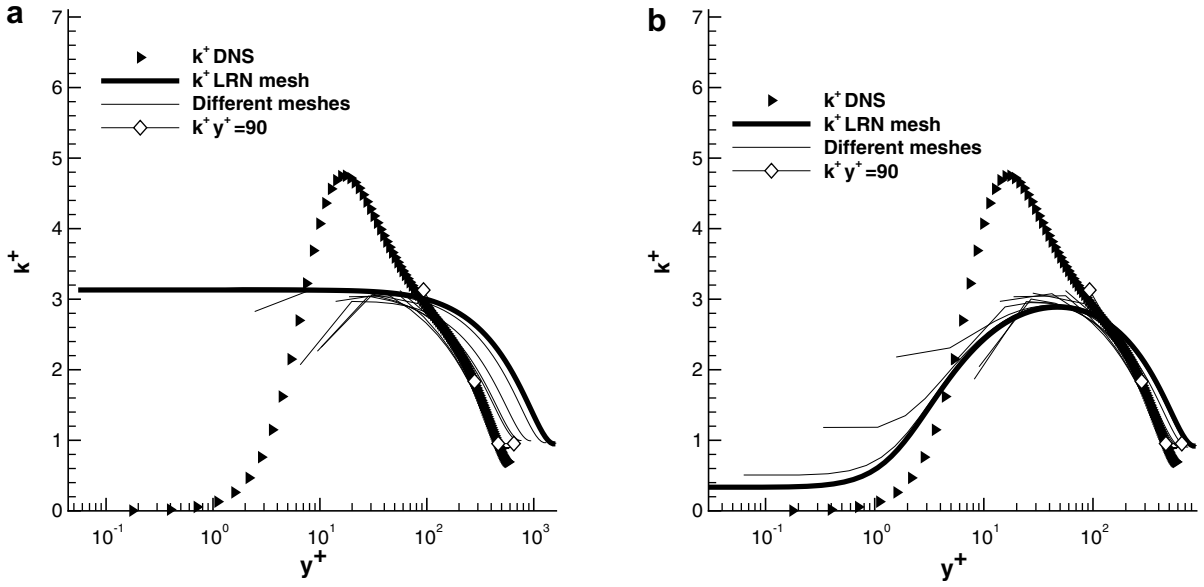

Fig. 8. Grid-sensitivity for the turbulent kinetic energy profile ($k^+ = k/u_\tau^2$) over wall distance ($y^+ = yu_\tau/\nu$) and comparison to DNS data [14]. Channel flow ($Re_\tau = 590$). (a) SWF1 model; (b) SWF2 model.

acceptable under $y^+ < 10$. Most probably explanation for this inaccuracy is the use of HRN k–ϵ in second and successive nodes, which are still placed in viscous areas for fine meshes.

On the other hand, k–ω approaches present a notoriously better behaviour. Fig. 7 shows a relatively small grid-sensitivity for both k–ω treatments. It seems reasonable to think that using the high Reynolds number k–ω model for inner nodes allow to improve accuracy. The ability of the ω-equation to provide both logarithmic and viscous sublayer solutions becomes important when the inner node is placed at viscous sublayer or buffer-layer. At the same time, Fig. 9 shows, specially with the WWF2 treatment, reasonably good turbulent kinetic energy predictions in comparison to DNS data [14]. This is an essential aspect in order to improve heat transfer accuracy. It is interesting to note that the turbulent sudden increases for the second wall cell for WWF1 computations (at near-wall nodes placed between $5 < y^+ < 20$). Pseudo-harmonic interpolation applied to obtain μ_t^n (Eq. (14)) seems to be responsible of this fact. While this strategy reduces shear stress and heat flux at near-wall nodes placed between $5 < y^+ < 20$ (trying to reproduce the wall-damping effect) the inner node suffers an increase of the turbulent viscosity, μ_t^N, due to this "numerical" stress reduction. However, this problem only appears in this thin region and the "numerical" stress reduction improves remarkably accuracy of the method in the overall of the turbulent boundary layer.

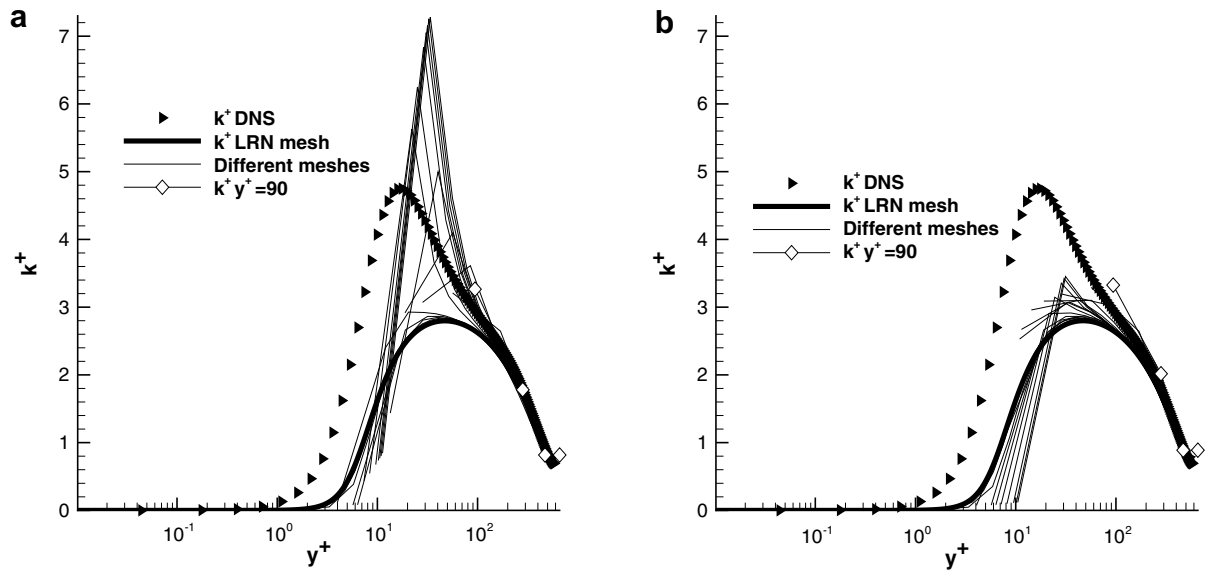

Fig. 9. Grid-sensitivity for the turbulent kinetic energy profile ($k^+ = k/u_\tau^2$) over wall distance ($y^+ = yu_\tau/\nu$) and comparison to DNS data [14]. Channel flow ($Re_\tau = 590$). (a) WWF1 model; (b) WWF2 model.

Table 5
SWF1 results

CV	y^+	y^*	C_f	Nu	C_f vs. EXP/DNS (%)	Nu vs. EXP (%)
160/(4.0s)	0.055	9.71e−2	4.19e−2	579.97	675.21	468.1
80/(4.0s)	0.115	2.04e−1	4.15e−2	587.51	668.29	475.48
100	8.244	12.044	1.18e−2	190.89	117.84	86.98
70	10.289	15.670	8.98e−3	153.71	66.25	50.56
40	14.026	24.170	5.45e−3	93.52	0.87	−8.39
10	56.037	99.023	5.43e−3	86.35	0.63	−15.42

Notation and exp. references: see caption in Table 8.

Table 6
SWF2 results

CV	y^+	y^*	C_f	Nu	C_f vs. EXP/DNS (%)	Nu vs. EXP (%)
160/(4.0s)	0.030	1.74e−2	1.25e−2	208.13	132.23	103.87
80/(4.0s)	0.063	4.50e−2	1.25e−2	212.68	131.04	108.33
100	8.244	12.044	1.18e−2	190.89	117.84	86.98
70	9.040	12.918	6.93e−3	119.71	28.34	17.26
40	14.026	24.170	5.45e−3	93.52	0.87	−8.39
10	56.037	99.023	5.43e−3	86.35	0.63	−15.42

Notation and exp. references: see caption in Table 8.

Table 7
WWF1 results

CV	y^+	y^*	C_f	Nu	C_f vs. EXP/DNS (%)	Nu vs. EXP (%)
320/(4.0s)	0.010	2.09e−7	6.08e−3	108.47	12.55	6.25
160/(4.0s)	0.021	1.38e−6	6.05e−3	109.43	12.11	7.19
100	5.698	1.587	5.62e−3	80.11	4.04	−21.53
60	9.633	7.924	5.78e−3	107.87	7.06	5.66
40	14.178	23.346	5.01e−3	95.99	−7.22	−5.98
10	56.376	101.011	5.50e−3	88.54	1.86	−13.28

Notation and exp. references: see caption in Table 8.

All treatments present very good agreement with DNS data [14] for near-wall cells placed at logarithmic region since they are using pure log-law for $y^+ > 30$. An overview of C_f grid-sensitivity of presented models can be followed in Tables 5–8.

As far as heat transfer is concerned, grid-sensitivity suffers an important increase. SWF1 and SWF2 present the same distorted behaviour as fluid flow predictions for near-wall cells placed at viscous regions, which was expected. As far as logarithmic areas is concerned, Nu var-

Table 8
WWF2 results

CV	y^+	y^*	C_f	Nu	C_f vs. EXP/DNS (%)	Nu vs. EXP (%)
320/(4.0s)	0.010	2.50e−7	6.08e−3	108.50	12.58	6.28
160/(4.0s)	0.021	1.38e−6	6.06e−3	109.55	12.26	7.31
100	5.698	1.587	5.62e−3	80.11	4.04	−21.53
60	9.506	3.160	5.63e−3	66.47	4.25	−34.89
40	14.314	24.621	5.67e−3	97.90	5.07	−4.1
10	56.613	102.707	5.55e−3	86.29	2.72	−15.48

Exp: $\frac{1}{\sqrt{f}} = 2.0\log Re_{D_h}\sqrt{f} - 0.8$, $(C_f = f/2)$, $Nu = 0.023Re_{D_h}^{0.8}\sigma^{0.4}$, (s) = Mesh stretching based on tanh function detailed in [16].

iability is much higher than corresponding C_f grid-sensitivity (see Tables 5 and 6). On the other hand, k–ω approaches also show a higher variability for Nu predictions in comparison to C_f results. The WWF1 model is able to achieve the smallest grid-sensitivity behaviour of all presented models, presumably thanks to wall-damping effect correction (see Tables 7 and 8). However, all approaches (even working on logarithmic near-wall cells) present inaccuracies approximately of 15% with respect to experimental Dittus–Boelter correlation (see caption in Table 8). Possible explanations can be found on assumptions applied (constant turbulent Prandtl number (σ_T), application of the"pee-function" [9] to obtain the law-of-the-wall for temperature, etc.). Further development has to be carried out in order to improve heat transfer predictions of all presented treatments.

4.2.2. LRN computations

With reference to LRN methods, Tables 9 and 10 present the grid study, as well as asymptotic results for WX93 and IL models, respectively. Fig. 10 presents velocity and turbulent kinetic energy predictions for both models using the finest mesh. Velocity predictions are similar to the ones obtained for WF techniques. Whilst, the ones related to k predictions, only the WX93 model seems to improve notoriously accuracy. A near-wall distance of $y^+ \approx 0.02$ needs to be achieved in order to obtain asymptotic results and verified predictions for both LRN models. This mesh requirement obviously implies important computational and CPU-time requirements. Table 11 offers a comparison between needed CPU times for different treatments. Model accuracy is approximately equal (using experimental and/or DNS data as references, all treatments are placed approximately in similar error range) and, on the contrary, CPU time consumptions for LRN techniques is considerably higher than the needed time for WF methods. Obviously, this is a very simple case, without separation, where WF techniques have been adjusted and where more general abilities of LRN techniques are not highlighted because of the simplicity of the flow. Additionally, presented CPU times for LRN techniques are related to verified predictions (see Section 3.2 and Tables 12 and 13), while WF simulations cannot ensure this point. Anyway and despite the simple case here treated, the quality of the mesh needed by LRN methods is an important handicap when solving fluid flow and heat transfer for engineering and industrial cases. The next test, the BFS flow, will present new features and this fact will be underlined again, bringing clarity to huge differences regarding computational requirements and their relationship to the accuracy of the predictions.

Table 9
WX93 results

CV	y^+	y^*	C_f	Nu	C_f vs. EXP/DNS (%)	Nu vs. EXP (%)
160/(4.0s)	0.021	1.73e−4	6.14e−3	110.47	13.70	8.20
80/(4.0s)	0.044	7.66e−4	6.12e−3	112.65	13.33	10.34
40/(4.0s)	0.097	3.86e−3	6.07e−3	116.08	12.41	13.70
20/(4.0s)	0.238	2.47e−2	5.84e−3	115.78	8.15	13.40
10/(4.0s)	0.701	2.70e−1	4.86e−3	94.40	−10.01	−7.54

Exp: $\frac{1}{\sqrt{f}} = 2.0\log Re_{D_h}\sqrt{f} - 0.8$, $(C_f = f/2)$, $Nu = 0.023Re_{D_h}^{0.8}\sigma^{0.4}$, (s) = Mesh stretching based on tanh function detailed in [16].

Table 10
IL results

CV	y^+	y^*	C_f	Nu	C_f vs. EXP/DNS (%)	Nu vs. EXP (%)
160/(4.0s)	0.019	2.87e−5	5.32e−3	96.68	−1.48	−5.30
80/(4.0s)	0.042	1.68e−4	5.59e−3	103.55	3.52	1.43
40/(4.0s)	0.100	1.56e−3	6.37e−3	121.96	17.96	19.46
20/(4.0s)	0.270	2.20e−2	7.47e−3	153.76	38.33	50.60
10/(4.0s)	0.898	5.01e−1	7.96e−3	183.48	47.41	79.71

Exp: $\frac{1}{\sqrt{f}} = 2.0\log Re_{D_h}\sqrt{f} - 0.8$, $(C_f = f/2)$, $Nu = 0.023Re_{D_h}^{0.8}\sigma^{0.4}$, (s) = Mesh stretching based on tanh function detailed in [16].

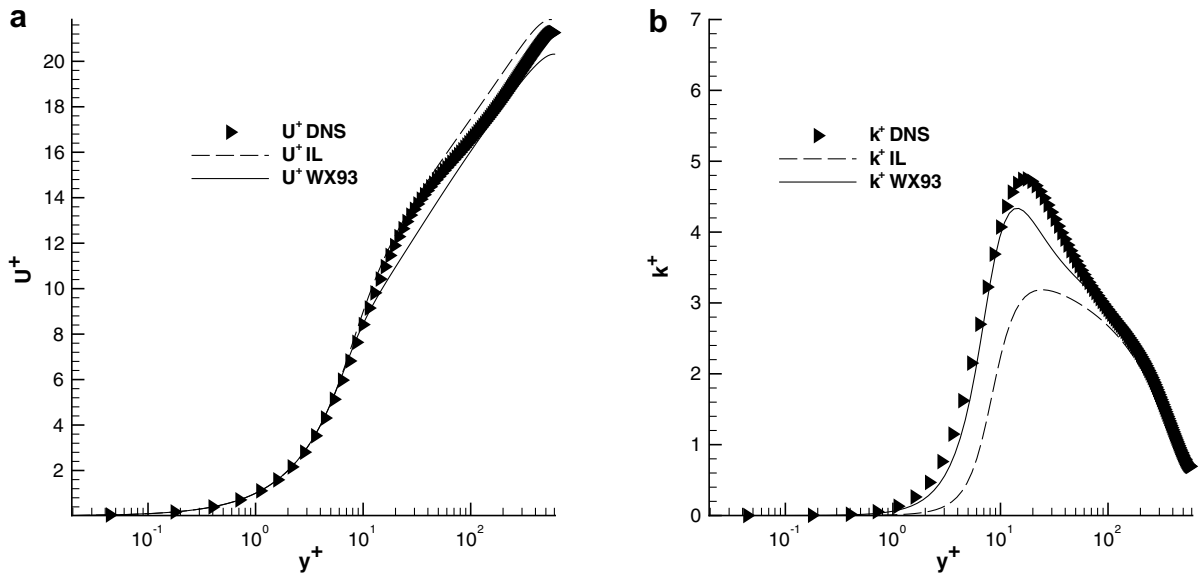

Fig. 10. (a) Velocity profile ($u^+ = u/u_\tau$) and (b) turbulent kinetic energy profile ($k^+ = k/u_\tau^2$) for IL and WX93 LRN models and comparison to DNS data [14]. Channel flow ($Re_\tau = 590$).

Table 11
Computational requirements and accuracy for different treatments

Model	CV normal dir.	CPU time (min)	C_f vs. EXP/DNS (%)	Nu vs. EXP (%)
SWF1	40*	1.49e−1	0.87	−8.39
SWF2	40*	1.49e−1	0.87	−8.39
WWF1	40*	8.05e−2	−7.22	−5.98
WWF2	40*	8.36e−2	5.07	−4.10
IL	160**	7.77e2	−1.48	−5.30
WX93	160**	6.11e2	13.70	8.20

Channel flow simulations $Re_\tau = 590$. (*) without mesh stretching; ** applying mesh stretching (see [16]). CPU characteristics: AMD Athlon 2600 Hz.

4.3. BFS flow

The proposed BFS case (Fig. 5b) contributes to the work by adding a test involving separated/reattached flow, geometrically complex and related to different wall grid meshing. This test case is important to assess turbulence models and modifications suggested herewith.

4.3.1. About the spatial discretization

As explained in Section 4.1, the coupled resolution of the development channel flow (to generate initial conditions) and the backward step has been carried out to simplify numerical computations and to check a more realistic test case, despite the increase of mesh requirements, specially for LRN treatments. For WF treatments, seven different meshes have been used to test grid-sensitivity of models. Fig. 12 exhibits y^+ obtained for several near-wall cells, using WWF2 treatment. The development channel is computed using a coarse near-to-wall region, with near-wall nodes located from $y^+ \approx 230$ (mesh m-2)

Table 12
WX93 convergence estimators for channel flow

Grid	$\bar{u}^* = \bar{u}/u_{in}$			$\overline{T}^* = \overline{T}/T_{in}$			$k^* = k/(0.03u_{in}^2)$		
$n_3/n_2/n_1$	Rn (%)	p	GCI* (%)	Rn (%)	p	GCI* (%)	Rn (%)	p	GCI* (%)
m0 m1 m2	78	1.7	8.5e−02	90	1.8	4.0e−02	72	2.1	1.0e+00
m1 m2 m3	93	2.1	1.6e−02	88	2.2	6.0e−03	78	1.8	4.5e−01
m2 m3 m4	88	1.9	9.2e−03	92	2.1	1.4e−03	76	2.1	9.0e−02

$Re_{D_h} = 43,000$.

Table 13
IL convergence estimators for channel flow

Grid	$\bar{u}^* = \bar{u}/u_{in}$			$\overline{T}^* = \overline{T}/T_{in}$			$k^* = k/(0.03u_{in}^2)$		
$n_3/n_2/n_1$	Rn (%)	p	GCI* (%)	Rn (%)	p	GCI* (%)	Rn (%)	p	GCI* (%)
m0 m1 m2	74	0.1	1.4e+01	50	0.4	4.7e−01	86	1.5	4.1e+00
m1 m2 m3	92	0.9	4.6e−01	94	0.4	3.7e−01	97	1.4	2.7e+00
m2 m3 m4	96	1.4	7.9e−02	99	1.4	3.0e−02	98	1.8	5.7e−01

$Re_{D_h} = 43,000$.

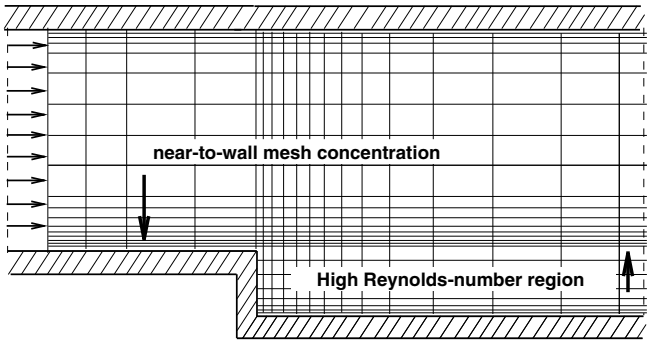

Fig. 11. BFS mesh qualitative description.

Table 14
Meshes for BFS case (axial X wall-normal)

Model	WF treatments	LRN IL	LRN WX93
m-2	$226 \times 44^{*}$	–	–
m-1	$226 \times 66^{*}$	–	–
m0	$226 \times 22^{**}$	$32 \times 24^{**}$	$32 \times 24^{**}$
m1	$226 \times 44^{**}$	$64 \times 48^{**}$	$64 \times 48^{**}$
m2	$226 \times 88^{**}$	$128 \times 96^{**}$	$128 \times 96^{**}$
m3	$226 \times 176^{**}$	$256 \times 192^{**}$	$256 \times 192^{**}$
m4	$226 \times 352^{**}$	$512 \times 384^{**}$	$512 \times 384^{**}$

* without mesh stretching; ** applying mesh stretching (see [16]).

up to near-wall cells placed at $y^+ \approx 11$ (mesh m4). As to the near-wall resolution of the area located downstream the step, mesh has been concentrated obtaining near-wall cells between $y^+ \approx 100$ and $y^+ \approx 0.5$, depending on the mesh. As can be observed, this set of simulations offers a wide range of placements for near-wall cells.

For LRN treatments, an important computational effort has been carried out to ensure the achievement of verified computations, following techniques explained in Section 3.2. Five different meshes for grid-refinement studies have been used. IL and WX93 models have needed very fine meshes, obtaining similar verifications estimators, and a relatively good accuracy. Because of the structure of the grid (Cartesian), mesh spacing applied on near-wall resolution for development channel is also applied on step downstream, where a high Reynolds number region takes place (see Fig. 11). This fact is essential to understand the present increase of the computational requirements related to LRN techniques, owing to the fine resolution needed by these techniques near the channel-wall and downstream step-wall. Table 14 summarises all meshes used to analyse BFS case.

4.3.2. WF computations

Tables 15–17 show performance of approaches to predict minimum C_f (in the recirculation bubble, where velocity has changed its sign), reattachment length (X_r^H) and maximum heat transfer, respectively, for WF approaches.

Using coarsest meshes (m-1, m-2), WWF1 and WWF2 treatments present a better behaviour than SWF1 and SWF2 approaches. This is in agreement with the observed smaller grid-sensitivity of k–ω approaches over channel flow, since such kinds of meshes (because there is flow separation and an increase of viscous effects at recirculation zone) present logarithmic and typical viscous near-wall cells.

As far as the finest meshes is concerned, k–ω approaches tend to the asymptotic results provided by the high Reynolds number k–ω model [5] (obtaining them at mesh m4). On the other hand, k–ϵ predictions are degraded when refining the mesh (which was expected due to their behav-

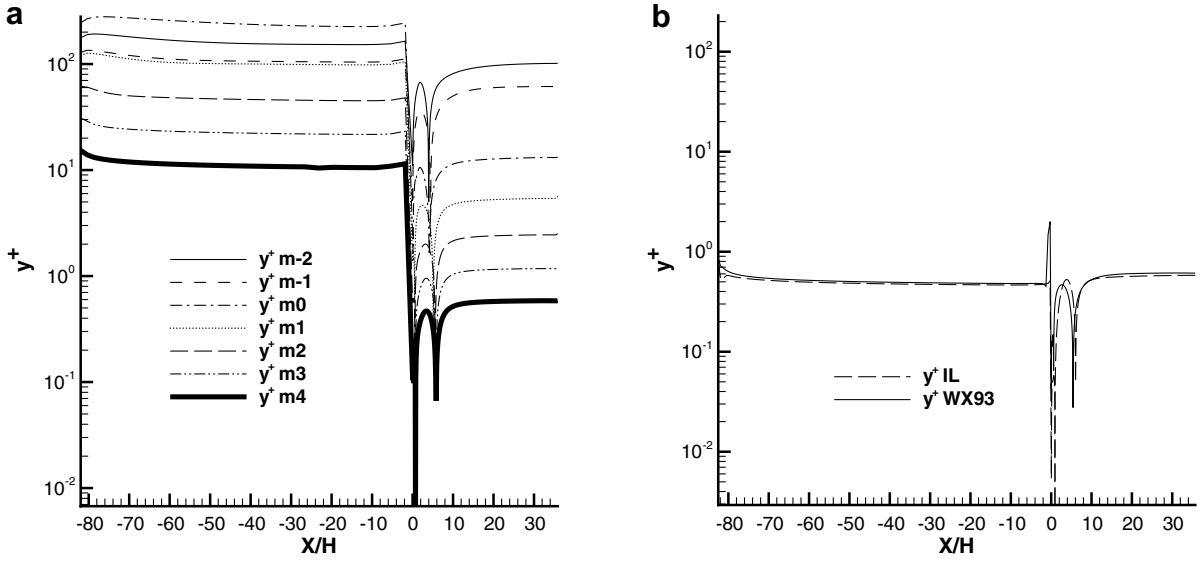

Fig. 12. Corresponding y^+ of near-wall cells for meshes used in BFS case: (a) WF meshes for WWF2 model; (b) finest LRN mesh (m4) for IL and WX93 models.

Table 15
BFS Min. C_f. Exp. Min $C_f = -1.020e{-}3$ [15]

Model	m-2	m-1	m0	m1	m2	m3	m4
SWF1	−1.260e−3	−1.072e−3	−1.929e−3	−2.480e−3	−4.075e−3	–	–
SWF2	−1.260e−3	−1.072e−3	−1.460e−3	−2.184e−3	−2.718e−3	–	–
WWF1	−1.281e−3	−1.114e−3	−1.333e−3	−1.465e−3	−1.346e−3	−1.381e−3	−1.407e−3
WWF2	−9.206e−4	−7.382e−4	−1.316e−3	−1.543e−3	−1.398e−3	−1.398e−3	−1.422e−3

Table 16
BFS reattachment $X_r^H = X_r/H$ Exp. $X_r^H = 6.26 \pm 0.1$ [15]

Model	m-2	m-1	m0	m1	m2	m3	m4
SWF1	3.12	3.64	3.06	4.07	4.79	–	–
SWF2	3.12	3.64	3.11	4.35	4.96	–	–
WWF1	4.49	4.86	4.29	5.27	5.65	5.72	5.92
WWF2	4.05	4.48	4.19	5.17	5.67	5.85	5.87

Table 17
BFS Max. *Nu*

Model	m-2	m-1	m0	m1	m2	m3	m4
SWF1	217.8	192.7	204.3	304.4	426.1	–	–
SWF2	217.8	192.7	206.1	254.2	321.3	–	–
WWF1	182.7	164.5	183.8	182.1	169.6	184.2	185.9
WWF2	165.4	143.8	182.3	140.3	165.8	183.3	185.2

iour using near-wall cells placed at viscous areas in channel flow test case). Consequently, predictions for m0 mesh present a strange behaviour (see Figs. 13 and 14) because of the mesh stretching applied to the wall and convergence have not been achieved for m3 and m4 meshes, where probably too many control volumes are placed in viscous areas.

Related to heat transfer, grid-sensitivity has been checked through the examination of *Nu* number. As shown, in Fig. 15, *Nu* grid-sensitivity for WWF1 treatment is reasonably small and much smaller than observed grid-sensitivity for k–ϵ methods. Results for the WWF2 model are close to the ones obtained for WWF1 (see Fig. 16), while the SWF1 *Nu* behaviour shows a higher grid-sensitivity than the SWF2 method, as can be seen in Table 17.

4.3.3. LRN computations

On the other hand, LRN models present a quite different behaviour. Again, as can be checked in Fig. 12, near-wall cells placed at $y^+ \approx 0.5$ in both walls (development channel and downstream of the step) to achieve asymptotic results and verified computations have been needed. This is the main reason to explain the extremely dense mesh used and the high CPU time needed for both simulations (see Table 18). Verification of numerical solutions has been analysed through methodology explained in Section 3.2. Tables 19 and 20 present verification estimators, and Table 21 shows the evolution of the reattachment length for WX93 and IL LRN models, respectively. This information demonstrates the achievement of asymptotic results (high percentage of Richardson nodes and orders of accuracy "p" close to theoretical ones), and ratifies the need of using such fine meshes. The distorted simulations for coarse meshes using the WX93 model is especially flagrant, where reattachment is underpredicted over 60%!. This fact is paradigmatic in order to understand the need of grid-refinement, as well as to show the previously known sensibility of

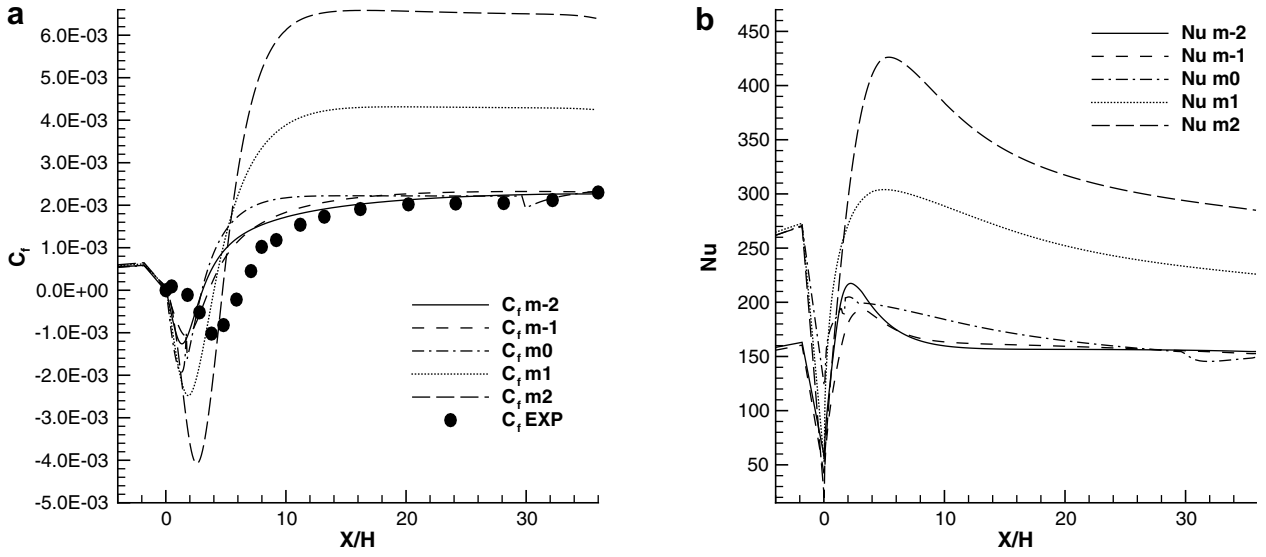

Fig. 13. SWF1 BFS simulations $Re_H = 37{,}500$: (a) skin friction ($C_f = \frac{\tau_w}{1/2\rho U_\infty}$); (b) Nusselt number ($Nu = \frac{q_w}{\lambda(T_w - T_{in})/3H}$).

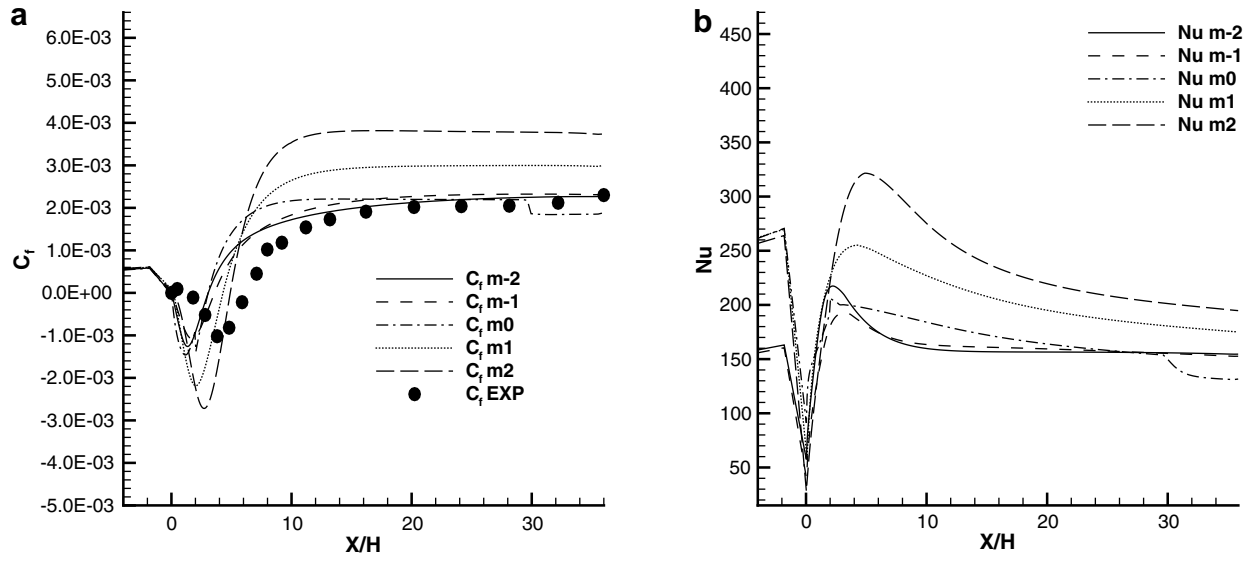

Fig. 14. SWF2 BFS simulations $Re_H = 37{,}500$: (a) skin friction ($C_f = \frac{\tau_w}{1/2\rho U_\infty}$); (b) Nusselt number ($Nu = \frac{q_w}{\lambda(T_w - T_{in})/3H}$).

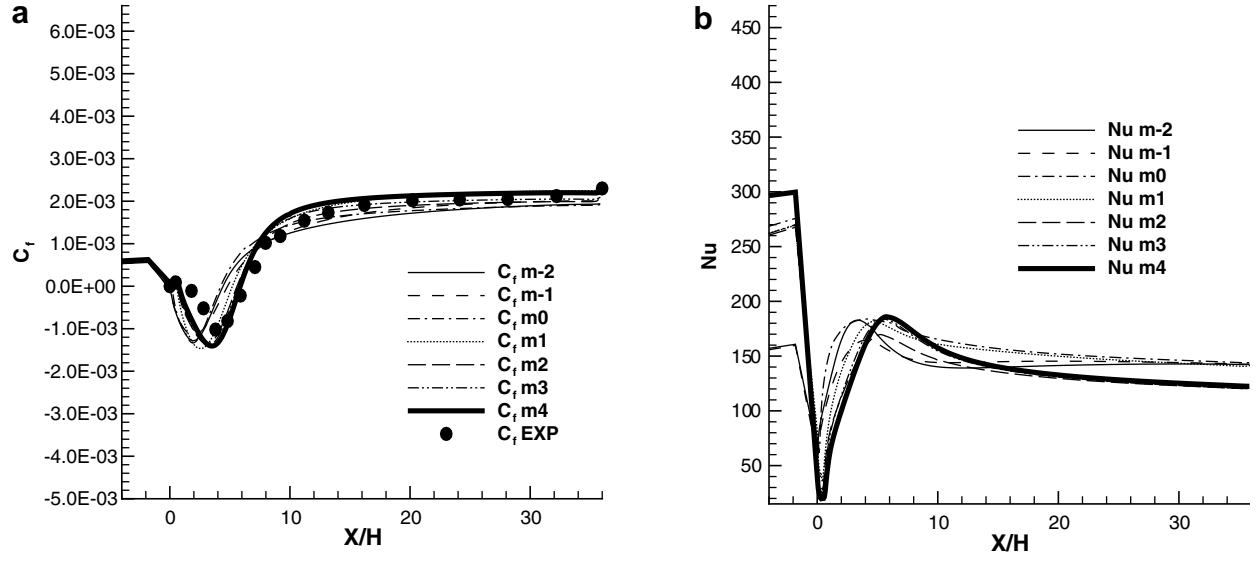

Fig. 15. WWF1 BFS simulations $Re_H = 37{,}500$: (a) skin friction ($C_f = \frac{\tau_w}{1/2\rho U_\infty}$); (b) Nusselt number ($Nu = \frac{q_w}{\lambda(T_w - T_{in})/3H}$).

ω-approaches to the near-wall mesh density. Related to accuracy, as shown in Fig. 17, C_f predictions are quite close to experimental results for both models: IL presents a very accurate reattachment length, while WX93 model shows a better minimum C_f in recirculation bubble. Both Nu predictions are quite similar, and also quite the same the ones obtained using finest meshes for WF k–ω approaches.

5. Concluding remarks

A critical study of different WF treatments have been presented. Considerations about turbulence modelling by means of k–ϵ and k–ω two-equation eddy-viscosity approaches have been carried out. Different strategies to improve detected grid-sensitivity for standard SWF1 treatment [3] have been proposed which are briefly described based on: enhancing ϵ profile using a two-layer integration to obtain ϵ_p and ϵ_N (SWF2 approach); changing dissipative variable from ϵ to ω (and also changing the HRN model used for inner nodes from k–ϵ [4] to k–ω [5]) (WWF1 approach) and, finally, designing a blending function to reduce grid-sensitivity on an ω platform (WWF2 approach). A rigorous grid-study has been carried out on channel and backward step flows. Both test cases have been useful to check model grid-sensitivity using a wide range of meshes, from extremely coarse to extremely fine grids. ω

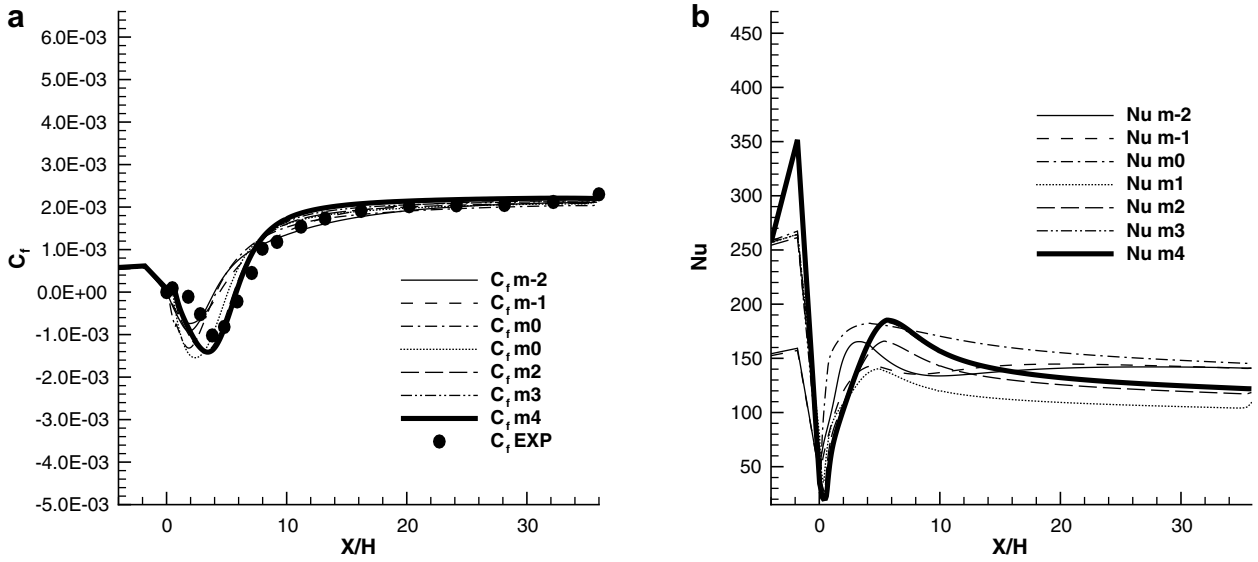

Fig. 16. WWF2 BFS simulations $Re_H = 37{,}500$: (a) skin friction ($C_f = \frac{\tau_w}{1/2\rho U_\infty}$); (b) Nusselt number ($Nu = \frac{q_w}{\lambda(T_w - T_{in})/3H}$).

Table 18
Computational requirements and accuracy for different treatments

Model	CV normal dir.	CPU time (min)	Reattachment length	Error vs. EXP (%)
SWF1	66*	86.17	3.64	−41.86
SWF2	66*	94.18	3.64	−41.86
WWF1	66*	24.98	4.86	−22.36
WWF2	66*	50.78	4.48	−28.43
IL	384**	3092	6.09	−2.71
WX93	384**	2985	5.45	−12.93

BFS flow simulations $Re_H = 37{,}500$. * without mesh stretching; ** applying mesh stretching (see [16]). CPU characteristics: AMD Athlon 2600 Hz.

approaches have presented better accuracy and smaller grid-sensitivity than ϵ treatments. However, all methods have shown poor abilities to predict accurate heat transfer rates, since assumptions to derive a law-of-the-wall for temperature seem to be too simple.

Table 21
Evolution of BFS reattachment with grid-refinement using IL and WX93 LRN models $X_r^H = X_r/H$ Exp. $X_r^H = 6.26 \pm 0.1$ [15]

Model	m0	m1	m2	m3	m4
IL	5.28	5.19	5.60	5.79	6.09
WX93	2.28	2.77	3.47	4.49	5.45

LRN computations have been carried out in order to compare accuracy and computational requirements when trying to solve present test cases. As can be seen, IL [6] and WX93 [7] models generally offer an improvement on accuracy, especially for the BFS case. This was expected since this test case is obviously more complex than the

Table 19
WX93 convergence estimators for BFS flow

Grid	$\bar{u}^* = \bar{u}/u_{in}$			$\overline{T}^* = \overline{T}/T_{in}$			$k^* = k/(0.03u_{in}^2)$		
$n_3/n_2/n_1$	Rn (%)	p	GCI*	Rn (%)	p	GCI* (%)	Rn (%)	p	GCI* (%)
m0 m1 m2	84	1.0	1.0e+00	58	2.4	8.3e−03	98	3.9	1.5e+00
m1 m2 m3	84	0.5	0.5e+00	92	1.4	2.1e−02	99	0.8	9.4e+00
m2 m3 m4	91	0.9	1.2e+00	89	1.4	8.7e−03	86	1.4	1.7e+00

$Re_H = 37{,}500$.

Table 20
IL convergence estimators for BFS flow

Grid	$\bar{u}^* = \bar{u}/u_{in}$			$\overline{T}^* = \overline{T}/T_{in}$			$k^* = k/(0.03u_{in}^2)$		
$n_3/n_2/n_1$	Rn (%)	p	GCI* (%)	Rn (%)	p	GCI* (%)	Rn (%)	p	GCI* (%)
m0 m1 m2	78	1.3	1.1e+00	75	3.0	3.3e−03	64	1.2	1.5e+00
m1 m2 m3	56	0.5	2.9e+00	51	1.2	9.3e−03	61	0.1	3.0e+01
m2 m3 m4	81	0.8	8.6e−01	80	0.4	4.3e−02	83	1.1	5.8e−01

$Re_H = 37{,}500$.

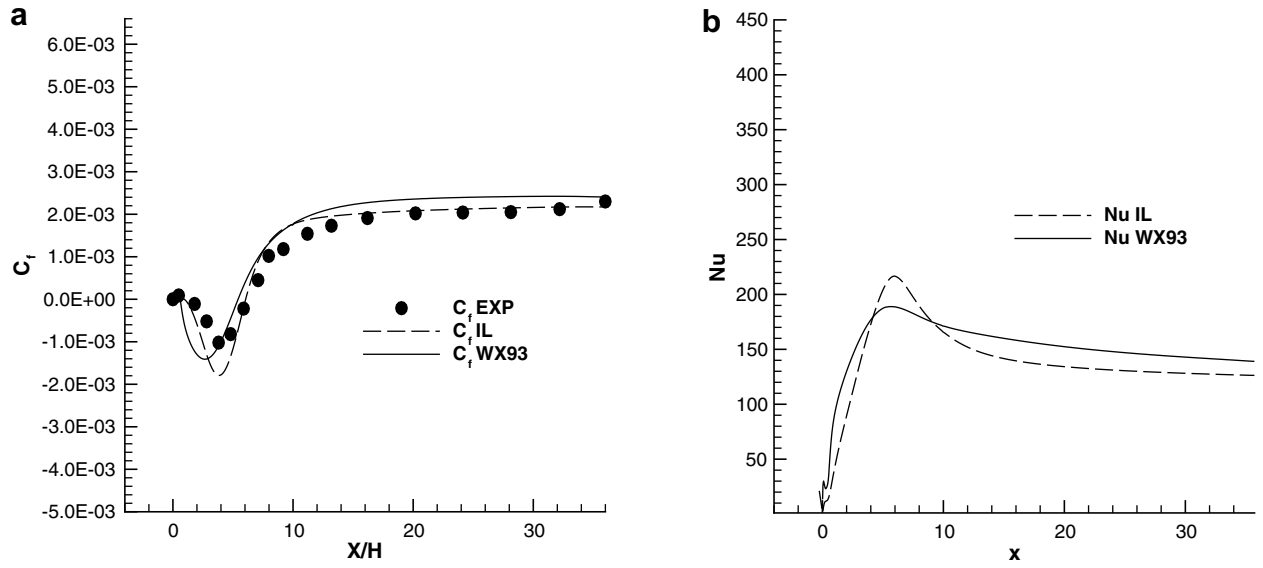

Fig. 17. IL and WX93 BFS simulations for m4 mesh $Re_H = 37{,}500$: (a) skin friction ($C_f = \frac{\tau_w}{1/2\rho U_\infty}$); (b) Nusselt number ($Nu = \frac{q_w}{\lambda(T_w - T_{in})/3H}$).

channel flow. However, this improvement has needed important computational requirements, implying very huge CPU time increases. In particular, the BFS case tested presents a complete configuration which becomes quintessential in order to quantify WF advantages in front of classical LRN methods. Present ω WF treatments advertise a flexibility which enable such treatments to obtain relatively accurate predictions while saving important computational requirements in comparison to LRN treatments.

Acknowledgements

This work has been financially supported by the Ministerio de Eduación y Ciencia, Secretaría de Estado de Universidades e Investigación, Spain (projects ENE2006-11099 CON and ENE2006-14247 ALT).

References

[1] T. Craft, A. Gerasimov, H. Iacovides, B. Launder, Progress in the generalization of wall-function treatments, Int. J. Heat Fluid Flow 23 (2002) 148–160.
[2] J. Bredberg, L. Davidson, Low-Reynolds number turbulence models: an approach for reducing mesh sensitivity, J. Fluids Eng. 126 (2004) 14–21.
[3] B.E. Launder, On the computation convective heat transfer in complex turbulents flows, J. Heat Transfer 110 (1988) 1112–1128.
[4] B. Launder, D. Spalding, The numerical computation of turbulent flows, Comput. Methods Appl. Mech. Eng. 3 (1974) 269–289.
[5] D.C. Wilcox, Reassessment of the scale-determining equation for advanced turbulence models, AIAA J. 26 (1988) 1299–1310.
[6] N. Ince, B. Launder, Computation of buoyancy-driven turbulent flows in rectangular enclosures, Int. J. Heat Fluid Flow 10 (1) (1989) 110–117.
[7] D.C. Wilcox, Simulation of transition with a two-equation turbulence model, AIAA J. 32 (1994) 247–255.
[9] C. Jayatillaka, The influence of Prandtl number and surface roughness on the resistance of the laminar sublayer to momentum and heat transfer, Progr. Heat Mass Transfer 1 (1) (1969) 193–329.
[10] J. Bredberg, Turbulence modelling for internal cooling of gas-turbine blades, Ph.D. thesis, Chalmers University of Technology, 2002.
[11] D. Wilcox, Turbulence Modeling for CFD, DCW Industries, Inc., CA, 1998.
[12] S.V. Patankar, Numerical Heat Transfer and Fluid Flow, Hemisphere Publishing Corporation, 1980.
[13] J. Cadafalch, C. Pérez-Segarra, R. Còsul, A. Oliva, Verification of finite volume computations on steady state fluid flow and heat transfer, J. Fluids Eng. 124 (2002) 11–21.
[14] R. Moser, J. Kim, N. Mansour, Direct numerical simulation of turbulent channel flow up to $Re_\tau = 590$, Phys. Fluids 11 (1999) 943–945.
[15] D. Driver, H. Seegmiller, Features of a reattaching turbulent shear layer in divergent channel flow, AIAA J. 23 (1985) 163–171.
[16] C. Pérez-Segarra, A. Oliva, M. Costa, F. Escanes, Numerical experiments in turbulent natural and mixed convection in internal flows, Int. J. Numer. Methods Heat Fluid Flow 5 (1) (1995) 13–33.